

<https://doi.org/10.1038/s41524-024-01218-5>

Tomography-based digital twin of Nd-Fe-B permanent magnets



Anton Bolyachkin^{1,2}✉, Ekaterina Dengina^{1,3}, Nikita Kulesh¹, Xin Tang^{1,2}, Hossein Sepehri-Amin^{1,3}, Tadakatsu Ohkubo¹ & Kazuhiro Hono^{1,3}

Many functional materials have been designed at the multiscale level. To properly simulate their physical properties, large and sophisticated computer models that can replicate microstructural features with nanometer-scale accuracy are required. This is the case for permanent magnets, which exhibit a long-standing problem of a significant offset between the simulated and experimental coercivities. To overcome this problem and resolve the Brown paradox, we propose an approach to construct large-scale finite element models based on the tomographic data from scanning electron microscopy. Our approach reconstructs a polycrystalline microstructure with actual shape, size, and packing of the grains as well as the individual regions of thin intergranular phase separated by triple junctions. Such a micromagnetic model can reproduce the experimental coercivity of ultrafine-grained Nd-Fe-B magnets along with its mechanism according to the angular dependence of coercivity. Furthermore, a remarkable role of thin triple junctions as nucleation centers for magnetization reversal is revealed. The developed digital twins of Nd-Fe-B permanent magnets can assist their optimization toward the ultimate coercivity, while the proposed tomography-based approach can be applied to a wide range of polycrystalline materials.

Permanent magnets are essential functional components of motors and generators in modern electric/hybrid vehicles, robotic systems, wind turbines, and other applications aimed at achieving carbon neutrality¹. In this high-tech sector, Nd-Fe-B magnets are dominant owing to their superior performance at room temperature. After the decades of research since the Nd₂Fe₁₄B compound was discovered^{2,3}, the maximum energy product of Nd-Fe-B magnets has almost reached its theoretical limit. However, the coercivity of industrial Nd-Fe-B magnets, which quantifies the resistance of a magnet to demagnetization in opposing magnetic fields, is still only 20–25% of its potential, as given by the anisotropy field ($\mu_0 H_a \sim 7.5$ T)^{4–6}. This discrepancy, known as the Brown paradox⁷, is mainly caused by microstructural imperfections and defects that promote the nucleation of reversed magnetic domains at magnetic fields much lower than H_a . To achieve a high coercivity, Nd-Fe-B magnets should comprise small Nd₂Fe₁₄B grains ($D < 1$ μ m) that are well aligned with *c*-axes and isolated from each other by a thin nonmagnetic intergranular phase (IGP), or at least by a weakly magnetic one^{5,6}. In addition, soft magnetic secondary phases should be eliminated, whereas grains on the magnet surface should be protected from any damage or strengthened such as by Dy diffusion⁸. The laborious optimization of Nd-Fe-B magnets toward the desired microstructure and

magnetic performance is still in progress^{9–16}. To accelerate this process, micromagnetic simulations are often used to elucidate the relationship between the microstructural features and macroscopic magnetic properties^{6,17–35}. Current micromagnetic models of Nd-Fe-B magnets address two cases of high practical importance: sintered magnets^{6,8,20–23} and hot-deformed ones^{24–33}.

Nd-Fe-B sintered magnets are composed of large equiaxial grains of sizes 3–5 μ m. Laguerre tessellation is commonly used to create a 3D model of such magnets. To make the model representative of a real sample, the tessellation parameters need to be adjusted, e.g., by varying until the power spectra of 2D slices of the model well reproduce the spectrum of a scanning electron microscope (SEM) image of the sample²⁰. The twins and crystallographic orientations of the grains can be incorporated into the model from SEM *via* electron backscatter diffraction²¹. However, micromagnetic models should have a spatial discretization of several nanometers to resolve the IGP and satisfy a constraint imposed by the exchange correlation length³⁶. Such a fine mesh is not feasible for sintered magnets even with state-of-the-art computational facilities. Either the models are significantly downscaled, e.g., by a ratio of 1:15 and even lower²¹, or the reduced order micromagnetic approach is used under certain assumptions, i.e., uniformly magnetized

¹Research Center for Magnetic and Spintronic Materials, NIMS, Tsukuba 305-0047, Japan. ²International Center for Young Scientists, NIMS, Tsukuba 305-0047, Japan. ³Graduate School of Science and Technology, University of Tsukuba, Tsukuba 305-8573, Japan. ✉e-mail: bolyachkin.anton@nims.go.jp

grains are considered which switching conditions are defined based on the embedded Stoner–Wohlfarth model^{8,18,20}.

Micromagnetic models of hot-deformed Nd-Fe-B magnets are less demanding in terms of meshing owing to their significantly smaller grain size^{24–33}. One of the largest finite element models (FEM) of hot-deformed magnets was $0.4 \times 0.4 \times 0.4 \mu\text{m}^3$ with an average lateral grain size of 77 nm ²⁸, whereas a finite difference model achieved $2 \times 2 \times 0.5 \mu\text{m}^3$ with a lateral grain size of 127 nm but under the ignorance of IGP (weakened direct exchange interaction between grains was prescribed instead)^{32,33}. The challenge for hot-deformed magnets is attributed to their typical microstructure – densely packed platelet grains with high aspect ratios – which is hard to mimic. Instead, a simplified layered stack of grains with Voronoi tessellation within each layer is often considered. Another drawback is that the intergranular phase is usually introduced as a solid region with uniform properties^{24–30}, despite recent experimental observations – IGPs at facets normal to the *c*-axis have lower transition metal content than those at the lateral facets, and thus lower magnetization^{9,13,34}. It is difficult to incorporate both realistic grain packing and IGP nonuniformities into current micromagnetic models. The resulting accumulation of assumptions leads to a commonly observed offset between the simulated and experimental coercivities for hot-deformed Nd-Fe-B magnets, as well as for sintered ones.

In this paper, we present large-scale finite element models of hot-deformed Nd-Fe-B magnets developed based on tomographic data. The proposed models can accurately reproduce the polycrystalline microstructure of real magnets overcoming the current limitations. In contrast to previous synthetic models, the intergranular phase was reconstructed as a set of thin individual regions localized between adjacent grains and isolated from each other by triple junctions (TJs). It allowed us to demonstrate the role of triple junctions in magnetization reversal and reach the stage at which the coercivity of hot-deformed magnets can be well reproduced in simulations. Such tomography-based digital twins of hot-deformed Nd-Fe-B magnets will promote optimization of the magnets toward ultimate coercivity.

Results

Development of tomography-based models

A hot-deformed Nd-Fe-B magnet with a nominal composition of $\text{Nd}_{13.4}\text{Fe}_{76.3}\text{Co}_{4.5}\text{Ga}_{0.5}\text{B}_{5.3}$ (at.%) and the typical microstructure was chosen to develop the tomography-based finite element model. The tomographic data was acquired as a series of SEM images while the sample surface was sequentially polished out using a focused ion beam (FIB)^{9,23}. The direction of collecting such slices (*x*-axis in Fig. 1a) was perpendicular to the *c*-axis crystallographic texture of the magnet, and the slicing step was 20 nm .

An area of $1.54 \times 1.54 \mu\text{m}^2$ was selected throughout the 78 FIB-SEM images to process a cubic volume. All images were manually segmented in a vectorized format so that each grain was represented by a set of polygonal

contours in several slices (Fig. 1b; grains are encoded by individual colors). The contours were then interpolated with an interpoint distance of $15\text{--}20 \text{ nm}$, which was comparable to the slicing step, while the last and first contours were additionally triangulated. The grains were thus converted into uniform point clouds distributed on their surfaces. The lists of neighboring grains were declared based on a 90 nm threshold for the minimum interpoint distance. Note that the collected SEM images after the manual segmentation provide a large dataset for training a deep learning model which will be able to speed up the processing for new samples.

The following routine was developed to construct 3D grains from their point clouds. First, axis-aligned minimum bounding boxes were created for each point cloud. These bounding boxes were scaled up by 1.2 with respect to their centers to fill artificial voids that may appear in the model along the *x*-axis due to the discrete step of FIB-SEM tomography (Fig. 1a). Second, a support vector machine (SVM) with a linear kernel was applied to pairwise separate all neighboring grains. Each grain was then constructed in 3D by cutting its bounding box with planes obtained after SVM, hereafter referred to as cutting planes (CPs). This ensured a close packing of the grains. Additionally, SVM suppressed point cloud distortions caused by drift during the FIB-SEM observations. One shortcoming was that only convex grains can be created in such a way, however this assumption seems to be appropriate for most grains in hot-deformed Nd-Fe-B magnets. As shown in Fig. 1c, the polycrystalline microstructure generated following the proposed routine corresponds well with the segmented SEM images.

It should be noted that the few-nanometer-thick intergranular phase could not be resolved in the SEM images. Therefore, an algorithm for IGP reconstruction was developed (Fig. 2a). For each pair of adjacent grains *i* and *j*, the corresponding CP with normal \mathbf{n}_{ij} was shifted in parallel in the depth of both grains by $t/2$, where *t* is the IGP thickness. These shifted CPs were used to trim the grains. The surfaces obtained after trimming were then extruded along the outward normals by *t* resulting in two overlapping volumes (Fig. 2a, middle image). Only the overlap was retained and assigned as the IGP between grains *i* and *j*. Figure 1c shows the model with thin IGP regions reconstructed in this way. Although the algorithm is simple, it offers various possibilities that have not been implemented previously. In contrast to the continuous IGP in synthetic models, the intergranular phase in our model was composed of individual regions. Therefore, the micromagnetic properties and thickness of the IGP can be varied locally in this model. Those parameters can also be correlated with the crystallographic orientations of contacting grains. Moreover, the space remaining after the construction of grains and IGP regions naturally introduced triple junctions into the model (inset of Fig. 1c).

To proceed with micromagnetic simulations, the model should be discretized in a high-quality mesh with a sufficiently small mesh size Δ to ensure at least one layer of internal nodes in thin IGPs ($\Delta \approx \sqrt{3/8t}$; see the inset in Fig. 1c). Therefore, small geometric entities should be eliminated

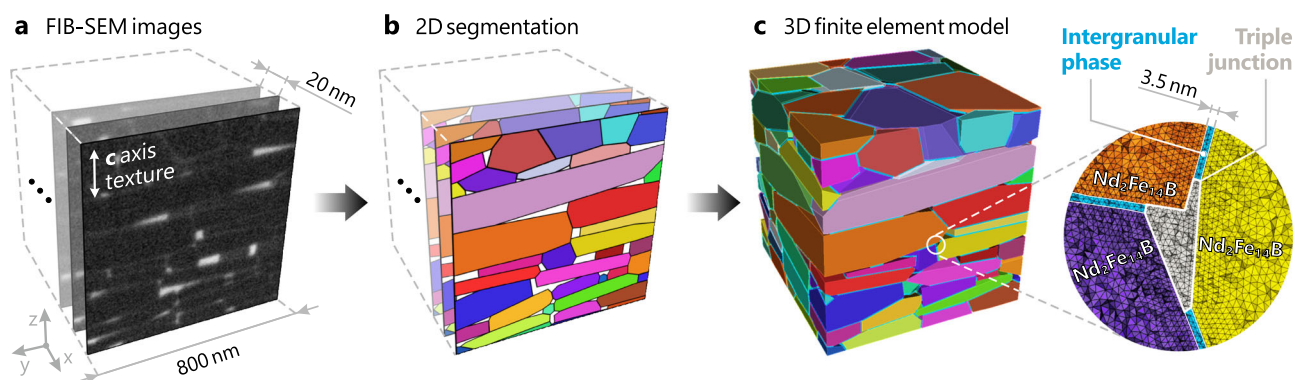


Fig. 1 | Development of a tomography-based model. **a** Acquisition of a series of FIB-SEM images for a hot-deformed Nd-Fe-B magnet (cropped area of $0.8 \times 0.8 \mu\text{m}^2$ is shown). **b** Processing of the images including 2D segmentation and the conversion

of grain slices into point clouds. **c** Generation of close-packed 3D convex grains isolated from each other by the intergranular phase. Triple junctions are made invisible except for a zoomed region showing the mesh around one of them.

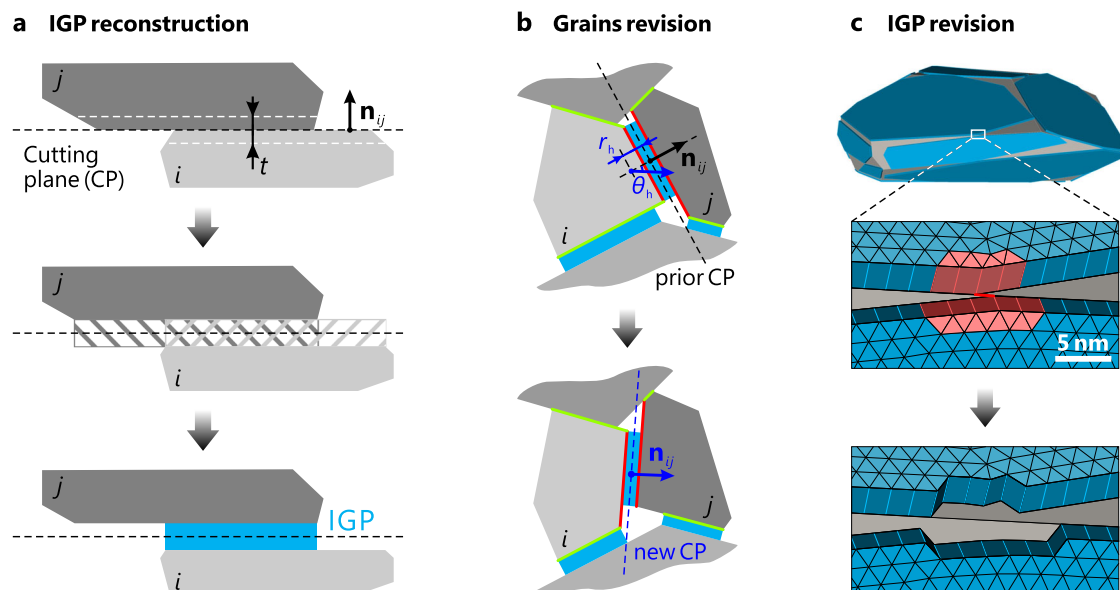


Fig. 2 | Geometry revisions for the tomography-based models. **a** Reconstruction of an intergranular phase (IGP) region between adjacent grains *i* and *j* (from top to bottom): parallel shifts of the cutting plane (CP) with the normal \mathbf{n}_{ij} in the depth of the grains by $t/2$, where t is the IGP thickness; trimming of the grains and extrusion of the obtained surfaces toward each other by t ; creating IGP as an overlap of the extruded volumes. **b** 2D schematic showing the correction of a grain *i*: \mathbf{n}_{ij} of a CP is

tilted randomly by a small angle θ_h while its origin is shifted by r_h . The correction is accepted if the total number of small geometric entities in surfaces associated with the revised CP (red) and all surrounding CPs (green) in both the grain and its neighbor decreases. **c** Elimination of a small entity that appeared due to the proximity of IGPs: IGPs are pre-meshed; then, mesh-based prisms are iteratively subtracted to avoid the formation of the small element.

before meshing, that are small curves ($l < \Delta$, where l is the curve length), small surfaces ($A < \sqrt{3}\Delta^2$, where A is the surface area), and narrow surfaces. This is typically the most challenging part of developing a finite element model. Furthermore, in the case of tomography-based models, such geometry revision should be gentle to preserve the microstructure retrieved from the FIB-SEM tomography as much as possible. In this study, we developed a two-stage approach to realize that.

The first stage is focused on the grains. It is applied when grains have been trimmed, but IGPs have not yet been introduced into the model. Let's consider a grain *i* with a small geometrical entity (Fig. 2b). To revise it, an appropriate CP should be selected first. For example, if the issue is a narrow surface, the selection is organized as follows: the surface is pre-meshed, and the worst triangular element with the highest aspect ratio (ratio of circumference and incircle radii) is found; then, one of the CPs surrounding the surface is randomly chosen with weight coefficients that are inversely proportional to the distances from the worst element to the CPs. After that, the normal \mathbf{n}_{ij} of the selected CP is tilted randomly by a small angle θ_h while its origin is shifted randomly by r_h along \mathbf{n}_{ij} – always with respect to the initial \mathbf{n}_{ij} after tomography. We used zero-mean normal distributions with standard deviations of $1\text{--}2^\circ$ and $1\text{--}1.5\Delta$ for θ_h and r_h , respectively. The correction is accepted, and the grains are updated if the total number of small geometric entities on the surfaces associated with the revising CP and surrounding CPs (red and green in Fig. 2b, respectively) in both the grain and its neighbor decreases. This procedure was repeated for all grains until all issues were resolved. When the grains were finalized, the IGPs were constructed, imprinted on the grain surfaces, and merged.

The second stage is dedicated to the revision of the IGPs. For a given IGP, the surfaces of adjacent grains were pre-meshed, and all triangular elements with a high aspect ratio (>2.5) were identified. Then, mesh-based prisms were iteratively subtracted from the IGP in the vicinity of the bad elements to avoid the formation of small entities that were causing them. Figure 2c shows an example of such elimination of a small curve that appears in the proximity of two IGPs. This procedure was performed for all IGP regions until a high-quality mesh was achieved for all grain surfaces. Finally, as the IGPs were revised, a triple junction region was created by subtracting the grains and IGPs from the model volume.

Microstructure and mesh of the models

Following the workflow described above, we prepared several tomography-based models of hot-deformed Nd-Fe-B magnets. In this study, the same thickness of 3.5 nm was prescribed for all IGPs. The largest model was based on the entire processed FIB-SEM tomography of $1.54 \times 1.54 \times 1.54 \mu\text{m}^3$. It consisted of 523 grains of their actual size and 2011 IGPs (Fig. 3a). This model was representative of a real magnet, i.e., 41% of the grains were internal grains whose shapes were not affected by the model boundaries. Arbitrarily aligned minimum bounding boxes (tight bounding boxes, TBB) were found for all grains to quantify their platelet shapes (inset of Fig. 3b). The grain width and height (maximum and minimum TBB edges), as well as their aspect ratio had mean values of 363 nm, 97 nm, and 3.9, respectively, with prominent standard deviations (Fig. 3b). TBBs were also used to assign easy magnetization axes (EAs) to grains since they are usually compressed along their *c*-axes after hot pressing. The details of this procedure are described in Supplementary Note 1.

To fit our computational facilities, five smaller models of $0.8 \times 0.8 \times 0.8 \mu\text{m}^3$ volume each were cropped from different places of the entire tomography (Fig. 3a). For example, Model 1 was discretized into 146×10^6 tetrahedral elements. The grains, IGPs, and TJs occupied 93.3, 3.9, and 2.8 vol.%, respectively, in this model. The triple junctions formed a rather complicated net-like structure (see Supplementary Fig. 2). Although the cropped models are smaller, their microstructural statistics are still in good agreement with those of the large model (Fig. 3b).

Micromagnetic simulations

We analyzed the dependence of coercivity (H_c) on the saturation magnetization (M_s) of the intergranular phase using the developed tomography-based models of hot-deformed Nd-Fe-B magnets (Fig. 4a). Although the ferromagnetic nature of IGP is justified, the actual value of $\mu_0 M_s$ is not well established; different experimental techniques provided estimations in the range of 0.4–1.1 T for sintered magnets^{6,37–40}. Therefore, we varied the IGP magnetization between 0–1.5 T to cover several possibilities in the simulations, while the IGP exchange stiffness was assumed to scale as $A \propto M_s^{2.17,34}$. To compare the simulated and experimental coercivities, the IGP $\mu_0 M_s$ of 0.8 T was selected as a potential reference. This M_s value is close to the

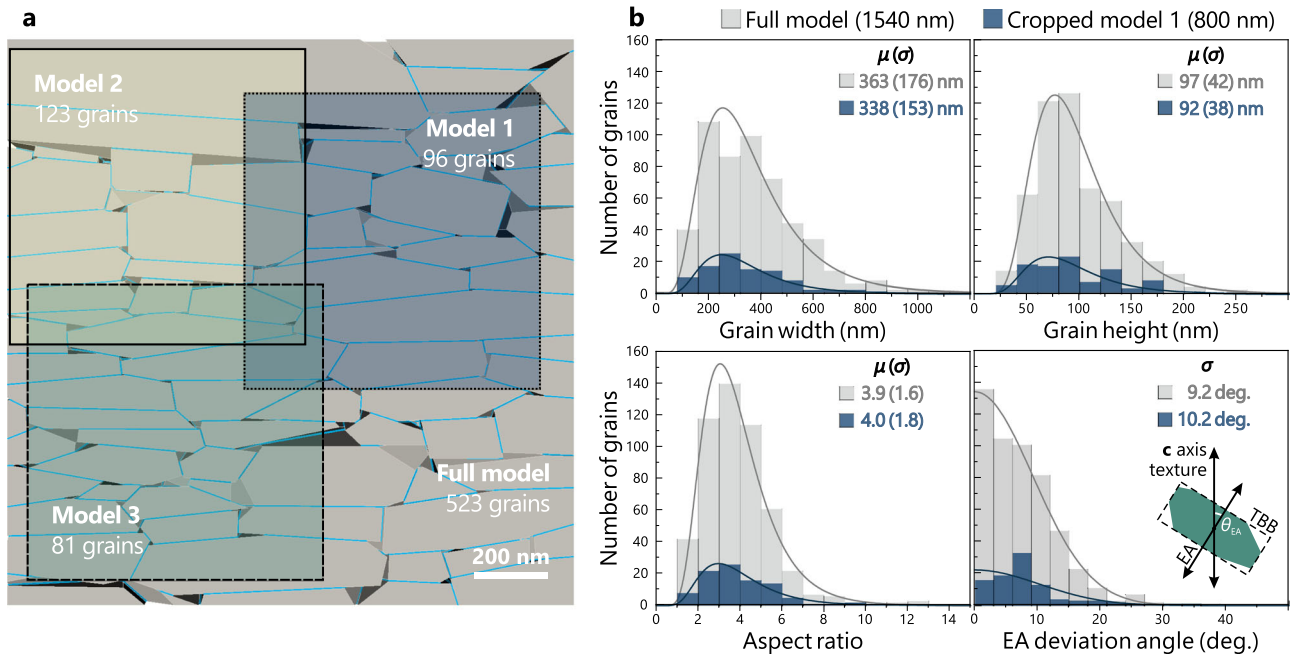


Fig. 3 | Microstructure of the tomography-based Nd-Fe-B models. **a** Side view of the large $1.54 \times 1.54 \mu\text{m}^2$ model and several cropped $0.8 \times 0.8 \mu\text{m}^2$ models used for micromagnetic simulations. **b** Histograms of the following microstructural features for the large model and one of the cropped models: the width and height of grain

according to its 3D tight bounding box (TBB), resulting aspect ratio, and easy magnetization axis (EA) inclination from the c-axis texture (EA of a platelet grain is defined based on its TBB; see the inset). Mean values (μ) and standard deviations (σ) are given for both models.

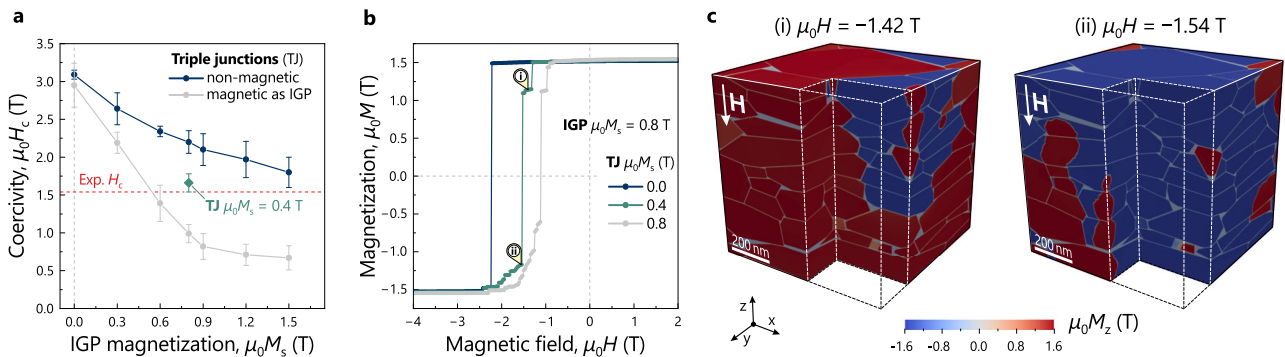


Fig. 4 | Micromagnetic simulations on hot-deformed Nd-Fe-B magnets. **a** Simulated coercivity vs. intergranular phase (IGP) magnetization for the models in which triple junctions (TJs) are either nonmagnetic or ferromagnetic as IGP. The experimental coercivity is indicated by a dashed line. Solid lines are eye guides.

b Demagnetization curves simulated for different magnetizations of TJs while the IGP magnetization is fixed. **c** Micromagnetic configurations before and after coercivity for the case when the magnetization of TJs was 0.4 T.

magnetization of Nd-Fe thin films containing approximately 70 at.% of Fe⁴¹; such films can be considered as IGP counterparts to some extent.

Two principal cases were analyzed for triple junctions. In an ideal case of nonmagnetic triple junctions, coercivity decreases monotonically from 3.1 ± 0.1 T to 1.8 ± 0.2 T as the IGP $\mu_0 M_s$ increases up to 1.5 T (Fig. 4a). The error bars represent the statistical uncertainties evaluated for different models. The coercivity is 2.2 ± 0.2 T for the IGP $\mu_0 M_s$ of 0.8 T. This is distinctly higher than the experimental coercivity of 1.54 T measured for this sample (Fig. 4a). In the second case, we considered ferromagnetic triple junctions whose magnetization followed the IGP M_s . In other words, IGPs and TJs were united in one phase with uniform magnetic properties (as usual IGP in synthetic models). It significantly changed the coercivity dependence that decreased rapidly from 3.0 ± 0.3 T to 0.7 ± 0.2 T with a more pronounced asymptotic behavior. The coercivity was 1.0 ± 0.1 T at the IGP $\mu_0 M_s$ of 0.8 T, which is significantly lower than the experimental value. Thick triple junctions with high magnetization act as strong nucleation sites

that promote magnetization reversal under relatively low magnetic fields. Although such a scenario is quite artificial for real magnets (unless they do not have a high content of soft magnetic secondary phases), it demonstrates the importance of realizing individual IGPs instead of the uniform one in the tomography-based models of Nd-Fe-B magnets.

Furthermore, the experimental coercivity confined between these simulated extreme cases led us to hypothesize that some triple junctions in Nd-Fe-B magnets, especially the thin ones, are ferromagnetic with M_s lower than that of the IGP. For example, if we consider the IGP $\mu_0 M_s$ of 0.8 T and the twice reduced magnetization of TJs, 0.4 T, the simulated coercivity of 1.7 ± 0.1 T approaches the experimental coercivity of 1.54 T (Fig. 4a). Figure 4b shows the demagnetization curves for this case and the extreme alternatives (TJs $\mu_0 M_s$ of 0.8 T and nonmagnetic one) for one of the models. TJs with twice reduced M_s still resulted in a remarkable decrease in the nucleation field from 2.22 T to 1.3 T. This was accompanied by appeared pinning of reversed magnetic domains. The micromagnetic configuration

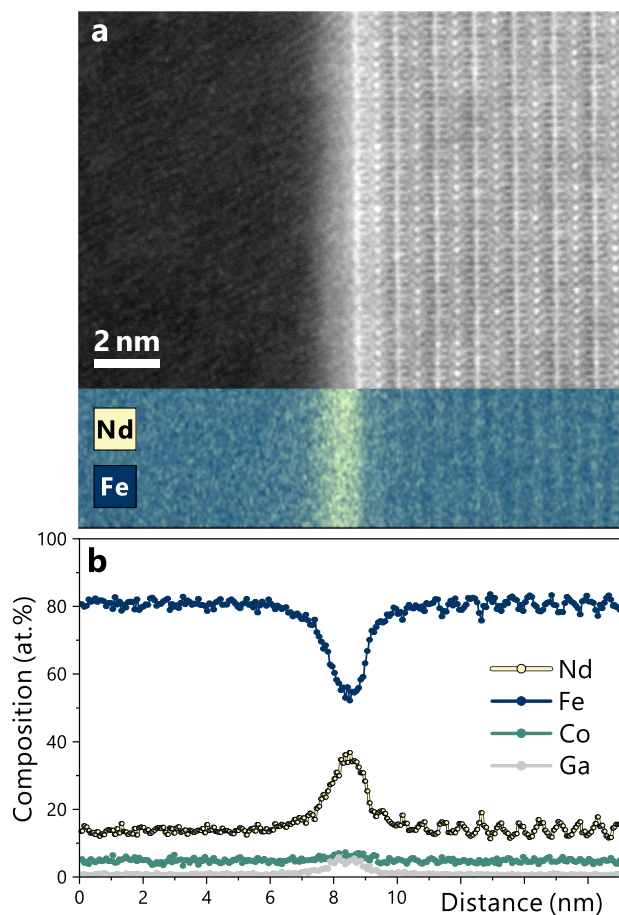


Fig. 5 | Composition of the intergranular phase. **a** High-resolution HAADF-STEM image and superimposed STEM-EDS map for a typical intergranular phase region in the hot-deformed Nd-Fe-B magnet for which FIB-SEM tomography was performed. **b** Composition line profile across the interface.

with such a pinned reversed domain is demonstrated in Fig. 4c, where the color code corresponds to the magnetization projection onto the applied magnetic field (z -axis). To further substantiate the proposed hypothesis regarding triple junctions and their role in magnetization reversal, scanning transmission electron microscopy (STEM) and atom probe tomography (APT) were conducted on the studied sample.

Chemical compositions of the intergranular phase and triple junctions

Figure 5a shows the high-angle annular dark field (HAADF)-STEM image and superimposed energy-dispersive X-ray spectroscopy (EDS) map for two $\text{Nd}_2(\text{Fe,Co})_{14}\text{B}$ grains separated by a thin amorphous intergranular phase. The (001) lattice planes were visible in the right grain. The composition line profile in Fig. 5b was extracted from the STEM-EDS map across the IGP interface. Such data were collected for eight different IGP regions, yielding the average concentrations of Nd, Fe, Co, and Ga of 33(3), 57(4), 6(1), and 4(1) at.%, respectively (standard deviations in parentheses). The intergranular phase was enriched in Nd and Ga and depleted in transition metals, although 63(4) at.% of Fe + Co is high enough to keep IGP ferromagnetic at room temperature⁴¹. Note that light elements, such as boron, could not be detected by STEM-EDS, leading to a minor overestimation of these concentrations.

Figure 6 shows a 3D atomic distribution map of Fe and Ga in the vicinity of a thin triple junction and two IGPs separating a few grains in the hot-deformed Nd-Fe-B magnet. The average concentrations of Nd, Fe, Co, and Ga in the intergranular phase were 25(2), 65(3), 6.0(0.2), and 1.2(0.2) at.%, respectively (statistics over five IGP regions in Fig. 6(i) and

Supplementary Fig. 3). The concentrations of Nd, Fe, Co, and Ga averaged over the triple junction volume were 51(3), 35(4), 9(1), and 5(1) at.%, respectively. The presence of B was negligible. Therefore, STEM-EDS can provide an unbiased evaluation of triple junctions that can be directly compared with APT data.

APT suggested a higher fraction of transition metals in IGP than STEM-EDS, whereas both methods were in good agreement regarding the spatial distribution of elements in thin triple junctions. A high-resolution STEM image of one of the TJs in the region where it was attached to an IGP is shown in Supplementary Fig. 4, along with EDS line profiles taken equidistantly over the region. The Nd content increased from 33 at.% with a gradient of 0.3 at.% nm^{-1} while moving from the IGP into the depth of the TJ, where the average concentrations of Nd, Fe, Co, and Ga become 50(3), 33(4), 10(1), and 7(1) at.%, respectively.

To enrich the statistics, a large area with various triple junctions was acquired using HAADF-STEM (Fig. 7a), and the chemical compositions were probed at the locations indicated by crosses in the corresponding STEM-EDS map (Fig. 7b). In Fig. 7c, the obtained compositions are represented by a bar chart ranked depending on the Nd content, whose values are given, as well as the atomic concentrations of Fe + Co. One can see that some thick triple junctions (e.g., at locations 1 and 2) were rich in Nd (>70 at.%). Such thick triple junctions are likely to be paramagnetic at room temperature since the Fe + Co content is below 30 at.%, which is considered as a threshold⁴¹. They can act as pinning sites for domain wall propagation. At the same time, a dozen relatively thin triple junctions have a moderate Nd content whereas Fe + Co occupies 40–58 at.%. Triple junctions with such compositions are expected to be ferromagnetic, with a reduced M_s compared to IGP. If their thickness is greater than the doubled exchange correlation length, they act as prominent nucleation sites and deteriorate the coercivity. Therefore, the STEM and APT observations are consistent with the conclusions from the tomography-based micromagnetic simulations regarding the magnetism of thin triple junctions.

Note that the STEM-EDS observations for some triple junctions may have a biased interpretation if they overlap with the grains. Such overlaps can be clearly observed when the grains have inclined facets (e.g., to the left of locations 8 and 11) – the contrast for Nd varies gradually in a diffusive manner. Therefore, the probing points shown in Fig. 7b were selected near the interfaces with prominent contrast changes.

Discussion

This study developed a large-scale tomography-based finite element model of hot-deformed Nd-Fe-B magnets that minimized microstructure-related assumptions. Consequently, the micromagnetic simulations can be performed with a significantly lower bias and uncertainty. This improvement is essential for addressing the problem of estimating the magnetic properties of the intergranular phase, e.g., by approximating the macroscopic hysteretic properties of magnets, such as coercivity. When the individual IGP regions and triple junctions were distinguished in the models, it was found that in addition to IGP, the magnetism of the triple junctions should also be considered to explain the coercivity of hot-deformed magnets. The content of Fe and Co in the relatively thin triple junctions is sufficiently high to keep them ferromagnetic at room temperature. Such triple junctions can be widely distributed in a magnet and serve as prominent nucleation sites for magnetization reversal – they are new factors in the search for “weak links” to coercivity¹⁸. At the same time, thick triple junctions are likely to be paramagnetic and contribute as pinning sites for the domain walls. Thus, assuming the triple junctions to be magnetic with 0.4 T saturation magnetization while the IGP $\mu_0 M_s$ was set to 0.8 T, we reproduced the experimental coercivity in micromagnetic simulations. However, a reasonable question arises as to whether it is just a quantitative match or the tomography-based model can describe the coercivity mechanism of hot-deformed magnets in general. To answer this question, we also performed simulations of the angular dependence of coercivity, which is commonly used to reveal the coercivity mechanism^{6,22,42–46}.

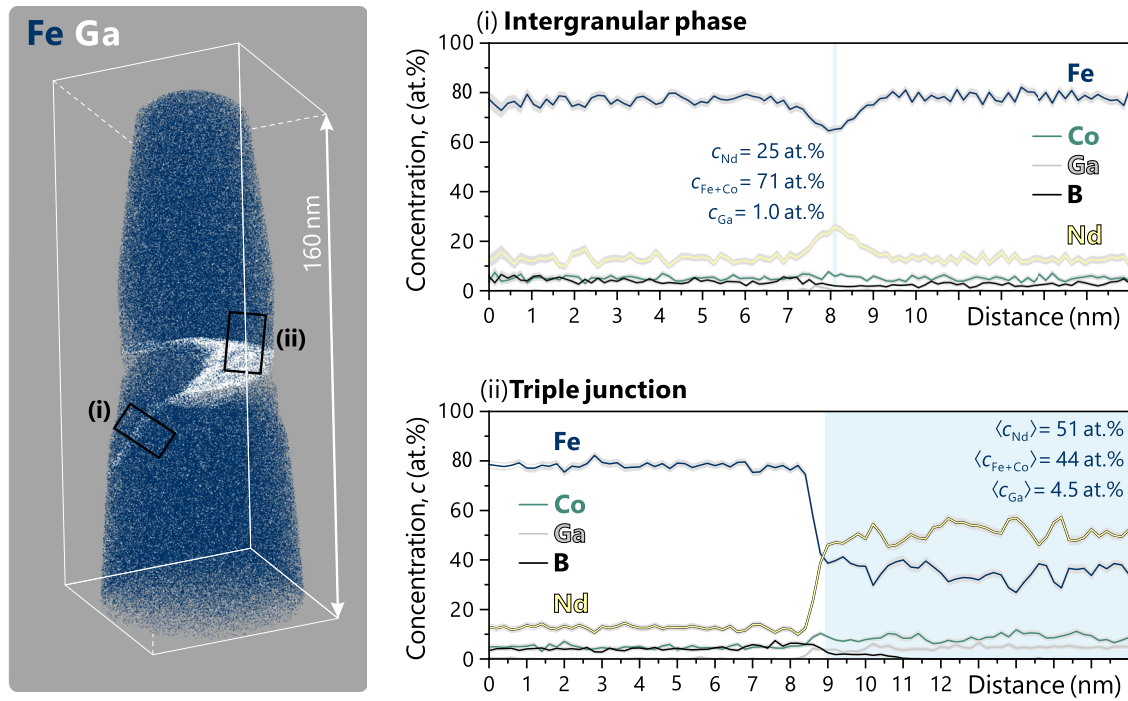


Fig. 6 | 3D atomic distribution map near a triple junction. Atomic map of Fe and Ga obtained from the hot-deformed magnet with the nominal composition of $Nd_{13.4}Fe_{76.3}Co_{4.5}Ga_{0.5}B_{5.3}$ and compositional profiles of the constituent elements calculated from volumes (i) and (ii) across the intergranular phase and a thin triple junction, respectively.

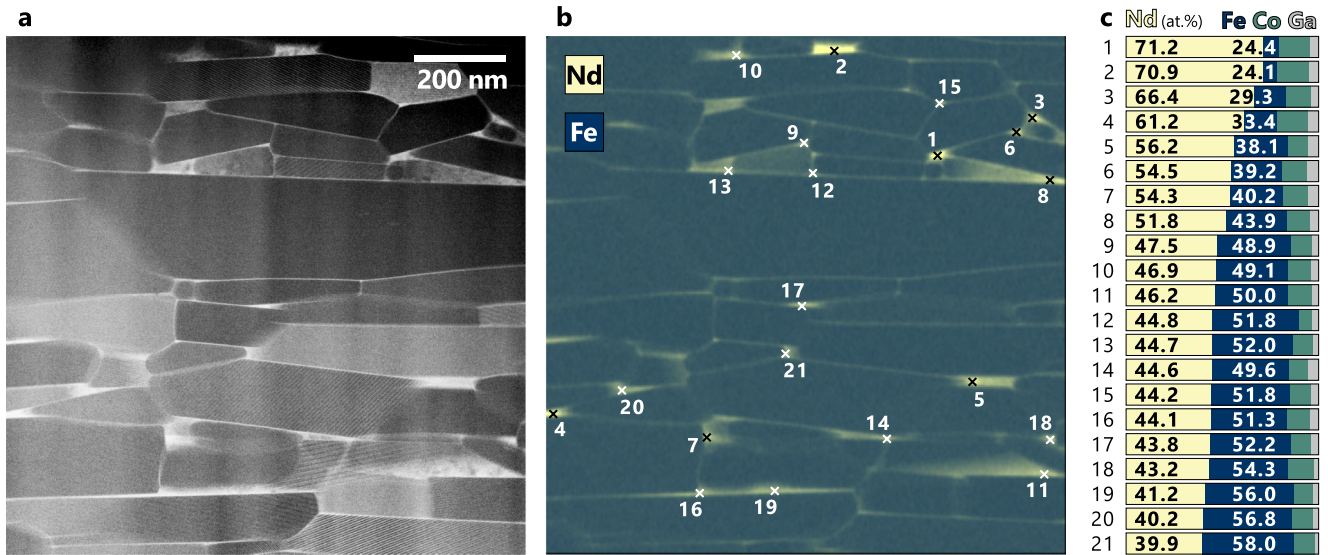


Fig. 7 | Compositions of the triple junctions. **a** Low-magnification HAADF-STEM image and **b** STEM-EDS map for the hot-deformed Nd-Fe-B magnet. Chemical compositions in different triple junctions were probed at locations indicated by crosses and ranked in **c** bar plots. Element content is proportional to the corresponding bar length, while the atomic concentrations of Nd and Fe + Co are given.

Figure 8 shows the simulated angular dependencies of coercivity, $H_c(\theta)$, for two cases: nonmagnetic triple junctions and weakly magnetic ones with 0.4 T saturation magnetization. Magnetization of the intergranular phase was set to 0.8 T in both cases. Here, θ denotes an angle between the c -axis texture and an applied external magnetic field H (inset in Fig. 8). Each angular dependence was normalized to the coercivity at $\theta = 0^\circ$. Solid lines indicate analytical dependencies attributed to pinning- and nucleation-type magnets within the Kondorsky^{47,48} and Stoner–Wohlfarth (SW)⁴⁹ models, respectively. Following Ref. 35, both analytical dependencies were adjusted to account for the distribution of

EAs within 2σ cone (18° , see Fig. 3b). Experimental $H_c(\theta)$ for this work and Ref. 35 are marked with crosses.

The nucleation-type angular dependence of coercivity with $dH_c/d\theta < 0$ at $\theta = 0^\circ$ and the minimum at $\theta \approx 30^\circ$ was obtained for the case of nonmagnetic triple junctions. This dependence diverged from the pinning-type experimental $H_c(\theta)$ with $dH_c/d\theta \geq 0$ at $\theta = 0^\circ$. When triple junctions were assumed to be weakly ferromagnetic, the angular dependencies of coercivity collected over different models for the statistics (Fig. 3a) split into two distinct trends – Fig. 8 shows the corresponding two $H_c(\theta)$ curves averaged over the models. The three models demonstrated no remarkable pinning

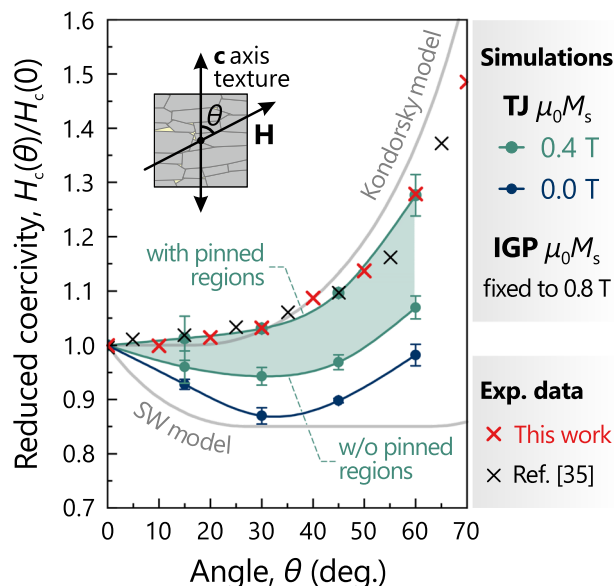


Fig. 8 | Coercivity mechanism in hot-deformed Nd-Fe-B magnets. Simulated angular dependencies of coercivity for the models with nonmagnetic triple junctions (TJs) and with TJs having a low magnetization of 0.4 T. The intergranular phase (IGP) magnetization is fixed at 0.8 T in both cases. $H_c(\theta)$ for weakly ferromagnetic TJs splits into two trends depending on whether or not domain wall pinning occurs during the magnetization reversal. Solid lines are guides to the eye, except for the theoretical $H_c(\theta)$ given by the Stoner–Wohlfarth (SW) and Kondorsky models. Experimental $H_c(\theta)$ is indicated by crosses.

during magnetization reversal. Their angular dependencies also followed the nucleation type, although they were closer to the experimental data. The two models with pinning at the reversal (e.g., see Fig. 4c) had remarkable pinning-type angular dependencies of coercivity, which were in good agreement with the experimental data. Apparently, the micromagnetic simulations of the larger model would have a much higher chance of encountering pinning; therefore, the obtained pinning-type $H_c(\theta)$ is more representative of a real magnet between these two trends. In previous simulations, such a pinning-type angular dependence was only possible after introducing a defective grain, e.g., a grain with a significantly reduced magnetic anisotropy constant^{6,22}. This magnetically softened grain acted as a low-field nucleation center, thereby enabling a domain wall pinning in the model. Weakly ferromagnetic thin triple junctions are supposed to be better candidates for this role. In this case, the pinning-type $H_c(\theta)$ can be naturally reproduced without artificial defects and be in good agreement with the experimental results.

In summary, we developed an approach for constructing large-scale finite element models of polycrystalline materials based on FIB-SEM tomography. In addition to reproducing the grain geometry and packing, special efforts were devoted to reconstructing thin intergranular phase regions separated by triple junctions. Such models with realistic microstructural features are crucial for accurately simulating the magnetic, mechanical, thermal, and other physical properties of a wide range of materials.

This approach was applied to ultrafine-grained hot-deformed Nd-Fe-B permanent magnets to address the long-standing problem of the remarkable discrepancy between simulated and experimental coercivities. Using micromagnetic simulations on such tomography-based models, we quantitatively reproduced the coercivity of hot-deformed Nd-Fe-B magnets and its pinning-type angular dependence. The key insight that allowed us to achieve good agreement with experiment is that thin triple junctions were considered as weakly ferromagnetic at room temperature. When the thickness of such junctions exceeded twice the exchange correlation length, they contributed to magnetization reversal as prominent nucleation sites, which also enabled domain wall pinning. The chemical compositions of

various triple junctions were investigated by APT and STEM-EDS, which showed relatively high Fe + Co contents in the thin triple junctions (40–58 at.%), supporting the above hypothesis.

Therefore, we established tomography-based digital twins of polycrystalline materials and demonstrated their benefits for hot-deformed Nd-Fe-B magnets. Such digital twins of Nd-Fe-B magnets can be further used to design their microstructure toward ultimate performance, while the concept itself can be adapted to other functional materials to enhance their optimization.

Methods

Sample preparation and magnetic properties measurement

A hot-deformed Nd-Fe-B magnet with the nominal composition of Nd_{13.4}Fe_{76.3}Co_{4.5}Ga_{0.5}B_{5.3} (at.%) was produced by induction melting of the constituent elements followed by melt-spinning, hot-pressing, and die-upsetting routines. Details of the synthesis are described elsewhere⁵⁰. The $M(H)$ demagnetization curves were measured at room temperature using a BH tracer after prior magnetization in a 7 T pulsed magnetic field. These measurements were performed at different tilting angles between the applied magnetic field and the c -axis crystallographic texture of the magnet. The coercivity at each angle was evaluated as the field at which the magnetic susceptibility (dM/dH) approached its maximum^{22,42}.

Microstructure characterization

A field emission scanning electron microscope Carl Zeiss CrossBeam 1540EsB was used to collect a series of 78 backscattered electron SEM images while the sample surface was sequentially polished out by a Ga FIB in steps of 20 nm^{9,23}. Such slicing was performed in a direction perpendicular to the c -axis crystallographic texture of the magnet.

The local chemical composition of the magnet was investigated by STEM and APT. The former was performed using an aberration-corrected FEI Titan G2 80-200 transmission electron microscope. A CAMECA LEAP5000 XS laser-assisted local electrode atom probe microscope was used for the APT. The samples for STEM and APT were prepared using the lift-out technique with a FEI Helios G4-UX dual ion beam system.

Tomography-based finite element model

The FIB-SEM tomography was segmented using CorelDRAW software, so that each grain was represented by a set of 2D polygonal contours. These data were transformed into uniform point clouds using a Python script. Then, lists of neighbors were obtained and the neighboring point clouds were separated by a linear support vector machine (Scikit-learn library). All the data were further used in the Coreform Cubit software, where the 3D polycrystalline microstructure was reconstructed using the Python-written routines described in the Results section. In this way, five models of $0.8 \times 0.8 \times 0.8 \mu\text{m}^3$ volume were developed from different locations of the processed tomography. The mean grain width and height were 363 (176) nm and 97 (42) nm, respectively. The thickness of the intergranular phase was set to 3.5 nm. Each model was discretized in $136\text{--}153 \times 10^6$ tetrahedral elements. The mesh size for the intergranular phase and triple junctions was 2.3 nm, whereas the mesh size for the grains gradually increased from 2.3 nm at the grain surfaces up to 5.0 nm toward their centers¹⁹.

Micromagnetic simulations

Demagnetization curves of the tomography-based models were simulated using the ‘b4vex’ code, which performs free energy minimization by a nonlinear conjugate gradient method⁵¹. All grains were considered to have magnetic properties of the Nd₂Fe₁₄B phase at room temperature as follows: saturation magnetization $\mu_0 M_s = 1.61$ T, uniaxial magnetic anisotropy constant $K_1 = 4.36$ MJ m⁻³, and exchange stiffness $A = 8$ pJ m⁻¹⁵². The easy magnetization axes were declared for the grains according to their spatial orientations, as described in Supplementary Note 1. The saturation magnetizations varied for both the intergranular phase and triple junctions, while their exchange stiffnesses were assumed to scale as $A \propto M_s^{2.17,34}$ with

respect to the Nd₂Fe₁₄B phase; their magnetic anisotropy was neglected ($K_1 = 0$). Two NVIDIA A100 GPUs with 160 Gb shared total memory were employed to conduct the micromagnetic simulations.

Data availability

The data supporting findings of this study are available from the corresponding author (A.B.) upon a reasonable request.

Code availability

The code for constructing the finite element model of a polycrystalline material based on its FIB-SEM tomography is available from the corresponding author (A.B.) upon a reasonable request.

Received: 21 August 2023; Accepted: 25 January 2024;

Published online: 12 February 2024

References

- Gutfleisch, O. et al. Magnetic materials and devices for the 21st century: stronger, lighter, and more energy efficient. *Adv. Mater.* **23**, 821–842 (2011).
- Sagawa, M., Fujimura, S., Togawa, N., Yamamoto, H. & Matsuura, Y. New material for permanent magnets on a base of Nd and Fe. *J. Appl. Phys.* **55**, 2083–2087 (1984).
- Croat, J. J., Herbst, J. F., Lee, R. W. & Pinkerton, F. E. Pr-Fe and Nd-Fe-based materials: a new class of high-performance permanent magnets. *J. Appl. Phys.* **55**, 2078–2082 (1984).
- Hono, K. & Sepehri-Amin, H. Strategy for high-coercivity Nd-Fe-B magnets. *Scr. Mater.* **67**, 530–535 (2012).
- Li, J., Sepehri-Amin, H., Sasaki, T., Ohkubo, T. & Hono, K. Most frequently asked questions about the coercivity of Nd-Fe-B permanent magnets. *Sci. Technol. Adv. Mater.* **22**, 386–403 (2021).
- Tang, Xin et al. Unveiling the origin of large coercivity in (Nd,Dy)-Fe-B sintered magnets. *NPG Asia Mater.* **15**, 50 (2023).
- Brown, W. F. Jr Virtues and weaknesses of the domain concept. *Rev. Mod. Phys.* **17**, 15–19 (1945).
- Exl, L. et al. Magnetic microstructure machine learning analysis. *J. Phys. Mater.* **2**, 014001 (2019).
- Sepehri-Amin, H., Une, Y., Ohkubo, T., Hono, K. & Sagawa, M. Microstructure of fine-grained Nd-Fe-B sintered magnets with high coercivity. *Scr. Mater.* **65**, 396–399 (2011).
- Sepehri-Amin, H. et al. High-coercivity ultrafine-grained anisotropic Nd-Fe-B magnets processed by hot deformation and the Nd-Cu grain boundary diffusion process. *Acta Mater.* **61**, 6622–6634 (2013).
- Sepehri-Amin, H., Ohkubo, T. & Hono, K. The mechanism of coercivity enhancement by the grain boundary diffusion process of Nd-Fe-B sintered magnets. *Acta Mater.* **61**, 1982–1990 (2013).
- Zhao, M. et al. Recent progress of grain boundary diffusion process for hot-deformed Nd-Fe-B magnets. *J. Rare Earths* **41**, 477–488 (2023).
- Tang, Xin et al. Coercivities of hot-deformed magnets processed from amorphous and nanocrystalline precursors. *Acta Mater.* **123**, 1–10 (2017).
- Vasilenko, D. Y. et al. Magnetics hysteresis properties and microstructure of high-energy (Nd,Dy)-Fe-B magnets with low oxygen content. *Phys. Met. Metallogr.* **122**, 1173–1182 (2021).
- Lambard, G., Sasaki, T. T., Sodeyama, K., Ohkubo, T. & Hono, K. Optimization of direct extrusion process for Nd-Fe-B magnets using active learning assisted by machine learning and Bayesian optimization. *Scr. Mater.* **209**, 114341 (2022).
- Wang, Z., Sasaki, T. T., Une, Y., Ohkubo, T. & Hono, K. Substantial coercivity enhancement in Dy-free Nd-Fe-B sintered magnet by Dy grain boundary diffusion. *Acta Mater.* **248**, 118774 (2023).
- Kovacs, A. et al. Computational design of rare-earth reduced permanent magnets. *Engineering* **6**, 148–153 (2020).
- Fischbacher, J. et al. Searching the weakest link: Demagnetizing fields and magnetization reversal in permanent magnets. *Scr. Mater.* **154**, 253–258 (2018).
- Fischbacher, J. et al. Micromagnetics of rare-earth efficient permanent magnets. *J. Phys. D Appl. Phys.* **51**, 193002 (2018).
- Kovacs, A. et al. Physics-informed machine learning combining experiment and simulation for the design of neodymium-iron-boron permanent magnets with reduced critical-elements content. *Front. Mater.* **9**, 1094055 (2023).
- Gusenbauer, M. et al. Extracting local nucleation fields in permanent magnets using machine learning. *NPJ Comput. Mater.* **6**, 89 (2020).
- Li, J. et al. Angular dependence and thermal stability of coercivity of Nd-rich Ga-doped Nd-Fe-B sintered magnet. *Acta Mater.* **187**, 66 (2020).
- Takeuchi, M. et al. Real picture of magnetic domain dynamics along the magnetic hysteresis curve inside an advanced permanent magnet. *NPG Asia Mater.* **14**, 70 (2022).
- Sepehri-Amin, H. et al. Microstructure and temperature dependent of coercivity of hot-deformed Nd-Fe-B magnets diffusion processed with Pr-Cu alloy. *Acta Mater.* **99**, 297–306 (2015).
- Wu, Y. et al. Microstructure, coercivity and thermal stability of nanostructured (Nd,Ce)-(Fe,Co)-B hot-compacted permanent magnets. *Acta Mater.* **235**, 118062 (2022).
- Liu, J. et al. Grain size dependence of coercivity of hot-deformed Nd-Fe-B anisotropic magnets. *Acta Mater.* **82**, 336–343 (2015).
- Li, J. et al. Coercivity and its thermal stability of Nd-Fe-B hot-deformed magnets enhanced by the eutectic grain boundary diffusion process. *Acta Mater.* **161**, 171–181 (2018).
- Tang, Xin et al. Thermally stable high coercivity Ce-substituted hot-deformed magnets with 20% Nd reduction. *Acta Mater.* **190**, 8–15 (2020).
- Tang, Xin et al. Relationship between the thermal stability of coercivity and the aspect ratio of grains in Nd-Fe-B magnets: experimental and numerical approaches. *Acta Mater.* **183**, 408–417 (2020).
- Wang, Z. et al. Correlation between the microstructure and magnetic configuration in coarse-grain inhibited hot-deformed Nd-Fe-B magnets. *Acta Mater.* **167**, 103–111 (2019).
- Hong, Y., Wang, G., Dempsey, N. M., Givord, D. & Zeng, D. Micromagnetic simulation of the effect of grain boundaries and secondary phases on the magnetic properties and recoil loops of hot-deformed NdFeB magnets. *J. Magn. Magn. Mater.* **491**, 165328 (2019).
- Tsukahara, H., Iwano, K., Ishikawa, T., Mitsumata, C. & Ono, K. Large-scale micromagnetic simulation of magnetization dynamics in a permanent magnet during the initial magnetization process. *Phys. Rev. Appl.* **11**, 014010 (2019).
- Tsukahara, H., Iwano, K., Ishikawa, T., Mitsumata, C. & Ono, K. Relationship between magnetic nucleation and the microstructure of a hot-deformed permanent magnet: micromagnetic simulation. *NPG Asia Mater.* **12**, 29 (2020).
- Zickler, G. A., Fidler, J., Bernardi, J., Schrefl, T. & Asali, A. A combined TEM/STEM and micromagnetic study of the anisotropic nature of grain boundaries and coercivity in Nd-Fe-B magnets. *Adv. Mater. Sci. Eng.* **2017**, 6412042 (2020).
- Bance, S. et al. Influence of defect thickness on the angular dependence of coercivity in rare-earth permanent magnets. *Appl. Phys. Lett.* **104**, 182408 (2014).
- Coey, J. M. D. *Micromagnetism, domains and hysteresis. In Magnetism and Magnetic Materials* 231–244 (Cambridge University Press, 2010).
- Nakamura, T. et al. Direct observation of ferromagnetism in grain boundary phase of Nd-Fe-B sintered magnet using soft X-ray magnetic circular dichroism. *Appl. Phys. Lett.* **105**, 202404 (2014).
- Kohashi, T., Motai, K., Nishiuchi, T. & Hirose, S. Magnetism in grain-boundary phase of a NdFeB sintered magnet studied by spin-

- polarized scanning electron microscopy. *Appl. Phys. Lett.* **104**, 232408 (2014).
39. Murakami, Y. et al. Magnetism of ultrathin intergranular boundary regions in Nd-Fe-B permanent magnets. *Acta Mater.* **71**, 370 (2014).
 40. Cho, Y. et al. Magnetic flux density measurements from grain boundary phase in 0.1 at% Ga-doped Nd-Fe-B sintered magnet. *Scr. Mater.* **178**, 533 (2020).
 41. Sakuma, A., Suzuki, T., Furuuchi, T., Shima, T. & Hono, K. Magnetism of Nd-Fe films as a model of grain boundary phase in Nd-Fe-B permanent magnets. *Appl. Phys. Express* **9**, 013002 (2016).
 42. Givord, D., Tenaud, P. & Viadieu, T. Angular dependence of coercivity in sintered magnets. *J. Magn. Magn. Mater.* **72**, 247 (1988).
 43. Kronmüller, H., Durst, K.-D. & Sagawa, M. Analysis of the magnetic hardening mechanism in RE-Fe-B permanent magnets. *J. Magn. Mater.* **74**, 291–302 (1988).
 44. Givord, D., Lu, Q., Rossignol, M. F., Tenaud, P. & Viadieu, T. Experimental approach to coercivity analysis in hard magnetic materials. *J. Magn. Magn. Mater.* **83**, 183–188 (1990).
 45. Li, J., Sepehri-Amin, H., Ohkubo, T. & Hono, K. Identifying the mechanism of hard magnet coercivity by its angular dependence. *Phys. Rev. B* **105**, 174432 (2022).
 46. Hayasaka, H., Nishino, M. & Miyashita, S. Microscopic study on the angular dependence of coercivity at zero and finite temperatures. *Phys. Rev. B* **105**, 224414 (2022).
 47. Kondorsky, E. J. On hysteresis of ferromagnets. *J. Exp. Theor. Phys.* **10**, 420 (1940).
 48. Urzhumtsev, A. N., Mal'tseva, V. E., Yarkov, V. Y. & Volegov, A. S. A modified Kondorsky model for describing the magnetization reversal processes in Nd-Fe-B permanent magnets. *Phys. Met. Metallogr.* **123**, 1054 (2022).
 49. Stoner, E. C. & Wohlfarth, E. P. A mechanism of magnetic hysteresis in heterogeneous alloys. *Philos. Trans. R. Soc. A* **240**, 599 (1948).
 50. Tang, Xin, Sepehri-Amin, H., Matsumoto, M., T. Ohkubo, T. & Hono, K. Role of Co on the magnetic properties of Ce-substituted Nd-Fe-B hot-deformed magnets. *Acta Mater.* **175**, 1–10 (2019).
 51. Fischbacher, J. et al. Nonlinear conjugate gradient methods in micromagnetics. *AIP Adv.* **7**, 045310 (2017).
 52. Hirotsawa, S. et al. Magnetization and magnetic anisotropy of $R_2Fe_{14}B$ measured on single crystals. *J. Appl. Phys.* **59**, 873 (1986).

Acknowledgements

This work was supported in part by the MEXT Program: Data Creation and Utilization-Type Material Research and Development Project (Digital Transformation Initiative Center for Magnetic Materials;

JPMXP1122715503) and JSPS KAKENHI Grant (JP23H01674). A.B. and X.T. acknowledge the International Center for Young Scientists (ICYS) at NIMS for providing ICYS fellowships.

Author contributions

X.T. performed FIB-SEM tomography and measured the magnetic properties of the Nd-Fe-B magnet. N.K., E.D., and A.B. segmented and processed the SEM images. A.B. conceptualized the development of a tomography-based finite element model, then it was realized in code by joint efforts of A.B., E.D., and N.K. TEM observations were performed by H.S. Micro-magnetic simulations were performed by A.B., then he wrote the manuscript while all the authors critically reviewed it. H.S., T.O., and K.H. supervised the work.

Competing interests

The authors declare no competing interests.

Additional information

Supplementary information The online version contains supplementary material available at <https://doi.org/10.1038/s41524-024-01218-5>.

Correspondence and requests for materials should be addressed to Anton Bolyachkin.

Reprints and permissions information is available at <http://www.nature.com/reprints>

Publisher's note Springer Nature remains neutral with regard to jurisdictional claims in published maps and institutional affiliations.

Open Access This article is licensed under a Creative Commons Attribution 4.0 International License, which permits use, sharing, adaptation, distribution and reproduction in any medium or format, as long as you give appropriate credit to the original author(s) and the source, provide a link to the Creative Commons licence, and indicate if changes were made. The images or other third party material in this article are included in the article's Creative Commons licence, unless indicated otherwise in a credit line to the material. If material is not included in the article's Creative Commons licence and your intended use is not permitted by statutory regulation or exceeds the permitted use, you will need to obtain permission directly from the copyright holder. To view a copy of this licence, visit <http://creativecommons.org/licenses/by/4.0/>.

© The Author(s) 2024